Natural Hazards (2023) 118:495–524
https://doi.org/10.1007/s11069-023-06015-9

ORIGINAL PAPER

Transparent soil model test and numerical study on the effect of adjacent spring on the stability of tunnel face in composite strata

Shaokun Ma[1] · Hongye Wei[1] · Zhibo Duan[1,2] · Ying Liu[1] · Zhen Huang[1] · Benfu He[1] · Zhang Zhou[1]

Received: 29 December 2022 / Accepted: 10 May 2023 / Published online: 26 May 2023

Abstract
To study the instability and failure mechanism of tunnel face in composite stratum and the evolution law of supporting pressure in the areas with spring, this paper used two different types of transparent soil and a self-designed 3D model test system. Six large transparent soil model tests were carried out by considering different confined water heads of spring and tunnel burial depth. The optical laser and high-speed camera were controlled to move on a high-precision linear platform. CT scanning was performed to obtain the failure model under different conditions. The finite element method considering a two-way fluid–structure coupling was used to validate the model test. The research results indicate under spring, the support pressure curves can be divided into three stages: rapid decline, rebound-rise, and constant. There is no rebound-rise stage under the condition of no spring. With increased confined water heads or reduced tunnel burial depth, limit support pressure shows an increasing trend. 2D and 3D damage models for different working conditions were obtained by PIV technology and 3D reconstruction technology. If there is a spring, the maximum displacement moves to the top of the tunnel with the increase of water head and the failure mode is a combination of "silo shape" and "inverted prism". When there is no spring, the maximum displacement appears at the interface of the soil layer, and the failure mode is a combination of "silo shape" and "wedge shape". The presence or absence of springs and the change of the confined water head have no significant effect on the height of the loosening area. With the tunnel burial depth ratio of 0.5 to 2.0, the height of the loose area increases from 0.17 to 0.83 D, and the soil arch area develops outward.

Keywords Spring · Transparent soil · Composite strata · Tunnel face stability · Model test · Finite element analysis

1 Introduction

At present, infrastructure construction is in the golden age of vigorous development, and many cities are building subway tunnels on a large scale. With the increasing subway mileage, shield tunnels often need to pass through areas in China with extremely developed

Extended author information available on the last page of the article

Fig. 1 Distribution map of Jinan subway

groundwater systems, such as Jinan City, Shandong Province, honored as "Spring City" as shown in Fig. 1 (Wang et al. 2019), and Tengchong City, Yunnan Province, honored as the "Land of Geothermal Energy" (Luo et al. 2019). Constructing subway shield tunnels in spring areas with such complex hydrogeological conditions is extremely important to ensure the stability of the shield tunnel face. The presence of spring along subway lines brings about unpredictable risks to the design, construction and operation of subway shield tunnels (Wang et al. 2017a, b; Sun et al. 2018). Any carelessness is very likely to result in the instability of the tunnel face, thereby triggering the occurrence of engineering accidents such as water burst, mud burst, and surface collapse (Li et al. 2016; Wang et al. 2017a, b, c). Therefore, the stability of shield tunnel face in areas with abundant spring has become a hotspot and difficult issue in urban construction.

In recent years, many researchers have carried out extensive model test studies on tunnel face stability in a homogeneous soil layer. The failure characteristics of tunnel face in sands were investigated through model tests with different tunnel burial depths ($C/D = 0.5$, 1 and 2). The results indicated that the ultimate support pressure increased with the increase of tunnel burial depth C/D, and a two-stage failure mode was proposed, i.e., local collapse and total collapse (Chen et al. 2013). To study the effect of the movement rate of tunnel face on the stability of tunnel face of shallow tunnels, a 1 g sand model test was carried out. It was found that the limit support pressure at a high movement speed is higher than that at a low movement speed, and soil failure occurred at the height above the inverted arch when the movement rate of the tunnel face was relatively high (Liu et al. 2018). The failure mechanism and limit support pressure for tunnel face under dry, non-drained, and steady seepage conditions were studied by nine sets of sand model tests. The results showed that the failure modes under different conditions were a combination of wedge and chimney shapes. However, the inclination angles of the lower wedges were all different, and the water level did not affect the failure mode of soil mass on the tunnel face under seepage conditions (Lu et al. 2018). Three sets of centrifugal model tests were conducted to study the effect of steady seepage of saturated sandy silt on the failure and limit support pressure of the tunnel face. The change of support pressure can be divided into two stages—sharp decrease and

slow linear increase. The limit support pressure shows a linear increase with the increase in groundwater head difference, and the soil failure mode in the limit state was composed of wedges and prisms (Chen et al. 2018).

Due to the complicated soil conditions in practical engineering, tunnel face stability in the composite strata is studied based on a homogeneous stratum. It was fined that the deformation and surface subsidence have significant difference between the dry sand mixed strata and general clay stratum, the deformation and surface subsidence vary rapidly, and the subsidence trough is "narrow and steep" in mixed strata (Zhang et al. 2020a, b).

Based on the principle of limit equilibrium, a calculation model for limit support pressure applicable to a composite stratum is proposed. It was demonstrated earlier that the shape of "loose area in unloading" was mainly determined by the properties of the upper soil layer, and the properties of the lower stratum determined the range and shape of areas with unsteady slippage (Sui et al. 2021). Six sets of model tests on transparent soil were carried out to study the failure model for the soil mass on tunnel face under different strata and burial depths. The test results indicated that the shape of the damaged body with shallow burial depth was the combination of pyramid and prism in the clay stratum. However, that with a large burial depth was the combination of the quadrangular pyramid and triangular prism. In the clay-gravel stratum, the shape of the damaged body with shallow burial depth was the combination of the wedge and inverted truncated pyramid, whereas that with high burial depth was the combination of wedge and prism (Ma et al. 2021a, b). Based on the silo principle, a calculation model for curved tunnels in composite stratum was proposed. The validation of the case analysis and numerical model showed that the soil mass on the tunnel face was subjected to asymmetric damage under the action of the eccentric support force. The limit support pressure first increased and then decreased with the decline curvature radius and leaned toward the outside of the curve (Dai et al. 2021). In order to determine the minimum support pressure on the excavation face of large shield tunnels in the rock–soil stratum, a new three-dimensional logarithmic spiral model (LS-M model) is proposed with acceptable accuracy and simpler implementation (Ding et al. 2022).

The above studies were primarily focused on saturated or anhydrous composite strata. However, there is often flowing groundwater below the impermeable stratum in actual scenarios. The previous research has shown that under the conditions with seepage and with no seepage, the failure modes of soil mass in front of the tunnel face were significantly different (Ma et al. 2021a, b). Researchers found that the pore-water pressure in front of the tunnel face decreases with the increasing opening area on the tunnel face and the increasing the ratio of vertical hydraulic conductivity to horizontal hydraulic conductivity though the centrifuge tests and numerical simulation (Yin et al. 2021). Based on the theory of fluid–solid coupling, the failure modes, deformation characteristics, and fluid–solid coupling effect in rock–soil were systematically investigated under different water levels, buried depths, tunnel diameters, and permeability coefficients when the excavation face was unstable (Chen et al. 2022).

At present, there are many studies on the stability of tunnel face under the condition of homogeneous stratum and composite stratum. However, studies on tunnel face stability in composite stratum under the seepage condition are sparse. In particularly, there are no reported findings on the effect of spring on the stability of tunnel face in the clay-gravel stratum. On this basis, the transparent soil test technology is adopted in this paper to study the instability mechanism and failure process of the shield tunnel face in the clay-gravel stratum under the condition of spring. Six large transparent soil physical model tests were conducted considering different confined water heads of spring and tunnel burial depth.

In combination with the 3D reconstruction test method, a three-dimensional failure model under the condition of spring was accurately obtained. Finally, the finite element analysis method considering two-way fluid–structure coupling was used to compare and verify the working conditions for corresponding model tests. This paper provides a theoretical reference for the design and construction of shield tunnels in areas with abundant springs.

2 Test equipment and system configuration

The model test system for studying the tunnel face stability is mainly composed of five parts: model tank of transparent soil, tunnel model, control system, liquid circulation system, and acquisition system, as shown in Fig. 2.

2.1 Model tank

Transparent soil material was used in this test. Since the price of high-purity fused quartz and transparent pore fluid is relatively high, an L-shaped glass partition was added inside the model casing to decrease the testing expenses and reduce the testing area as much as possible. The size of the model tank used in the study was 850 mm × 230 mm × 750 mm (length × width × height). The front face of the model box was made of reinforced glass to ensure that the camera could capture images of different sections.

2.2 Tunnel model

Based on axial symmetry, a semi-structural model with a similarity ratio of 1:50 was used for the tunnel. The tunnel had an outer diameter of 120 mm, an inner diameter of 108 mm, and a rigid plate in the front. The exterior of the tunnel model was fixed on the reinforced glass by fixed ring walls and stainless steel bolts. Inside the tunnel model, a servo motor, lead screw, linear bearing, and tension–compression force sensor were connected by a connecting rod, driving the rigid plate forward and backward. In addition, due to the strong corrosiveness of pore fluid, all parts of the tunnel model are made of stainless steel material.

2.3 Control system

Based on the displacement control method, a control tank was used to control the servo motor, which controlled the rigid plate to move forward and backward and realized the active and passive failures of the shield tunnel face. In addition, the moving direction and speed of the rigid plate can be controlled in real time, with the speed control range of 0.00–50.00 mm/min.

2.4 Fluid circulation system

Simulating the spring is crucial for studying the effect of spring on the stability of the shield tunnel face. In this test, an L-shaped pipe was arranged in front of the rigid plate to simulate the spring. Meanwhile, the spring with different confined water heads was simulated by changing the location height of the head control barrel and the liquid level in the

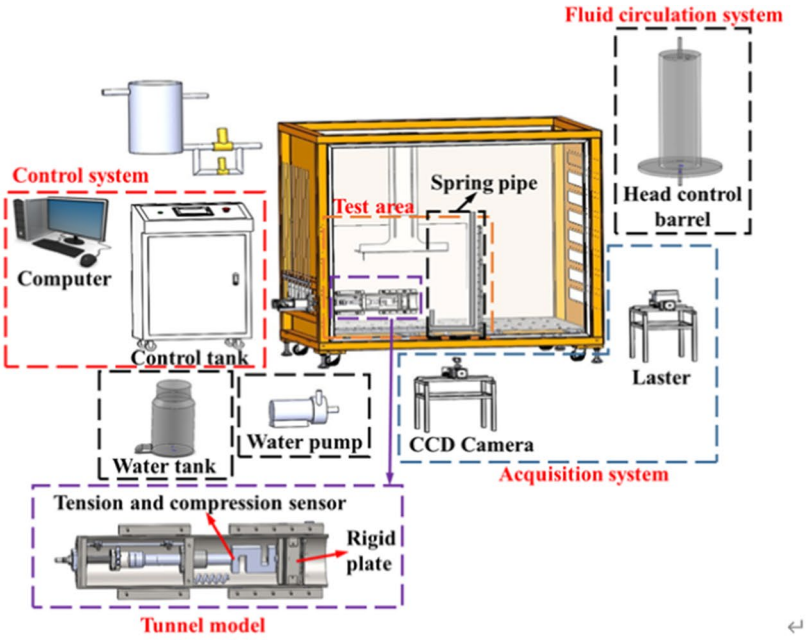

(a) Schematic sketch of the physical model test

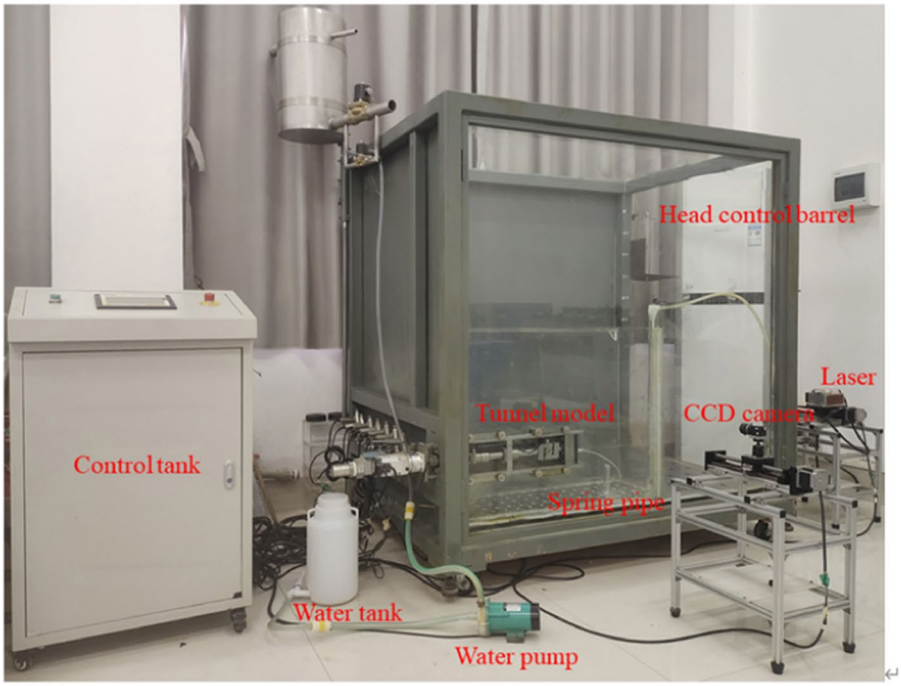

(b) Test apparatus

Fig. 2 Physical model test

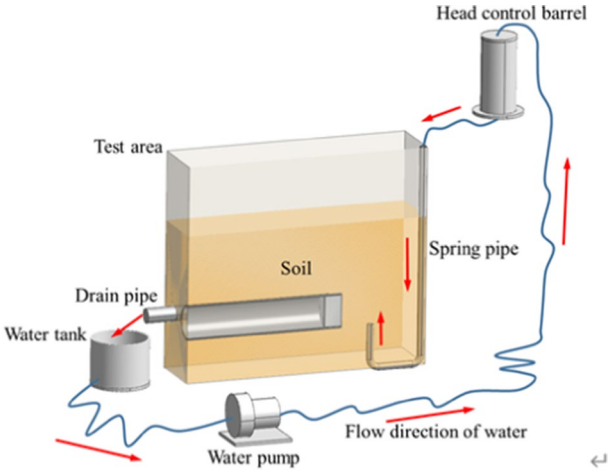

Fig. 3 Diagram of liquid circulation system

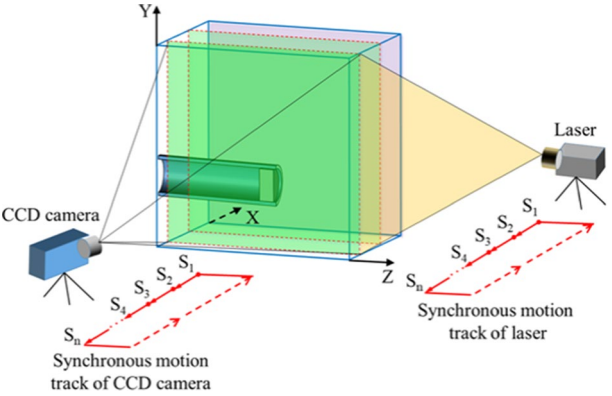

Fig. 4 Synchronous motion of CCD camera and laser

barrel. In addition, pore fluid is recycled in the test, with the circulation process of pore fluid shown in Fig. 3.

2.5 Acquisition system

The acquisition systems include a data acquisition system and an image acquisition system. The data acquisition system could monitor the support pressure of the tunnel face in real time. The image acquisition system comprised a CCD industrial camera with a lens focal length of 8 mm, a laser with an output power of 8 W, and two high-precision linear control platforms. On the high-precision linear platform, the industrial camera and the laser move synchronously along *x*-direction at a speed of 1 mm/s, stop every 5 mm, and the camera starts to capture images, thereby obtaining images of different slices positions under the same horizontal displacement of the rigid plate. The PIV technology is used to process the images with different states acquired at the same slice location and then obtain the displacement field of each slice location and, finally, obtain the 3D spatial deformation of the stratum through the self-compiled 3D reconstruction program. The synchronous motion track is shown in Fig. 4.

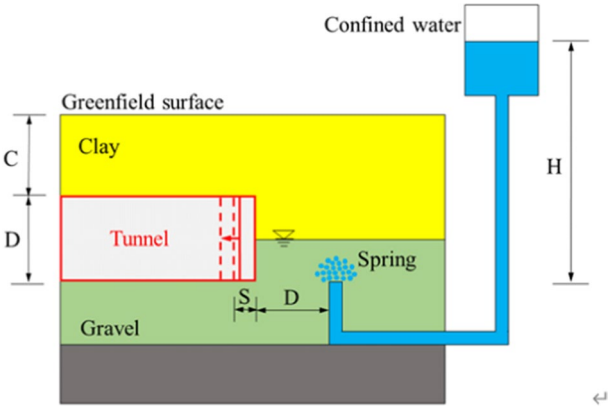

Fig. 5 Test diagrams and simulation schemes

Table 1 Test schemes

	Schemes	Stratum	Burial depth C/Tunnel diameter D	Spring head/mm	Pipe diameter (mm)
Test schemes	1	Clay-Gravel	2.0	Not spring	–
	2	Clay-Gravel	2.0	5D	6.00
	3	Clay-Gravel	2.0	7D	6.00
	4	Clay-Gravel	2.0	9D	6.00
	5	Clay-Gravel	1.0	5D	6.00
	6	Clay-Gravel	0.5	5D	6.00

3 Test preparation and process

3.1 Test schemes

This paper mainly studies the failure mechanism and limit support pressure of tunnel face under the condition of spring with different confined water heads and different tunnel burial depth. Based on the transparent soil technology, six model tests are carried out, with the specific dimensions and test schemes shown in Fig. 5 and Table 1. In Fig. 5, S is defined as the back displacement of rigid excavation plate, C is defined as burial depth, D is defined as tunnel diameter, H is defined as the water head difference between the exposed spring water and the external head control barrel.

The height of the confined water is adjustable in the model test. During the whole test, the spring outlet is always at the center section of the tunnel, but the height of the spring water pipe and the head control barrel can be adjusted. The groundwater bearing head in the gravel formation is generally above 10 m. Therefore, the larger heads of 5D, 7D and 9D are selected to prevent external factors such as head loss during the test, so as to ensure the model test effect.

3.2 Preparation of transparent clay

Laponite RD is a new type of transparent clay material, which has been widely applied in experimental geotechnical research (Chini et al. 2015; Zhang et al. 2020a, b; Ma et al. 2021a, b). First, Laponite RD powder was mixed with deionized water at a mass ratio of 4:96, and the basic mechanical parameters such as shear strength, consolidation coefficient, and compressibility coefficient were obtained through the cross-plate shear test, consolidation test, and variable head permeability test as shown in Table 2 (Wallace and Rutherford 2015; Tian 2018). The results show that Laponite RD transparent clay has macroscopic geotechnical properties similar to soft clay; thus, it can be used as a substitute for soft clay in geotechnical physical model tests.

Laponite RD is prone to flocculation in water, so deionized water with conductivity less than 0.1 μs/cm was used in the test. Laponite RD was mixed with deionized water in proportion. To facilitate the later PIV image analysis, it is necessary to add PSP tracer particles with a particle diameter of 50 μm. The configuration process of the transparent clay is shown in Fig. 6.

3.3 Preparation of transparent gravel soil

Transparent gravel soil was composed of synthetic aggregates with the pore fluid whose refractive index matches that of the aggregate. In terms of synthetic aggregate, Liu and Iskander (2010) and Iskander et al. (2002) carried out mechanical tests on the transparent gravel soil prepared with amorphous silica gel, fused quartz, or glass sand and found that these materials could better simulate natural sand to a certain extent. However, fused quartz has certain advantages over other granular materials, together with very small compressibility. Regarding most current pore fluids, their main disadvantages are high viscosity and temperature sensitivity, making it difficult to ensure the transparent property of the gravel soil during the test. Therefore, a new pore fluid was selected in this test. It was composed of sodium thiosulfate and sodium iodide (Carvalho et al. 2015). The pore fluid was prepared by mixing sodium iodide particles and ultrapure water at the mass ratio 0.552:0.448, with the refractive index adjusted to 1.4590 (Zhao et al. 2010; Liu et al. 2020). Figure 7 shows the preparation procedure of pore fluid.

Table 2 General material properties

Parameter	Value
Reported shipped water content, %	< 10
Measured shipped water content, %	8.32
Refractive index	1.5
Specific gravity	2.53
Bulk density, g/cm^2	0.908
Liquid limit, LL	1150
Plasticity index, PI	910
Permeability coefficient, cm s^{-1}	$0.405–1.14\times10^{-7}$
Compressibility coefficient, MPa^{-1}	88–939
Consolidation coefficient, cm^2 s^{-1}	$3.555–13.520\times10^{-6}$
Cohesion, kPa	0.555
Internal friction angle, °	11.034

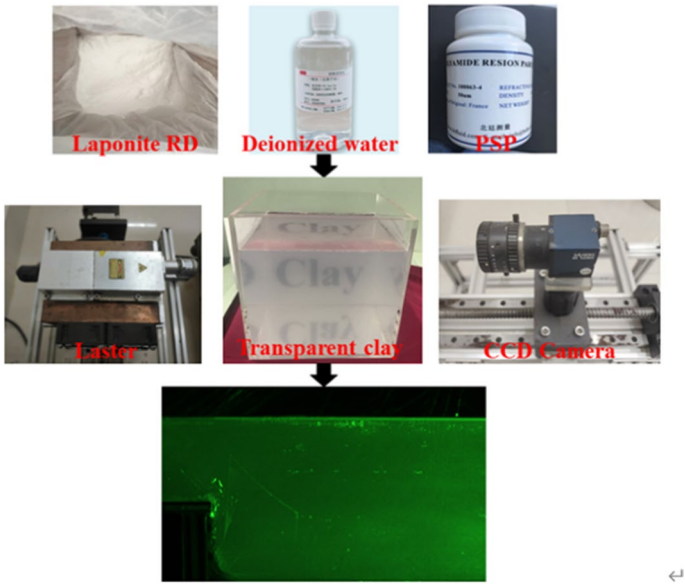

Fig. 6 Transparent clay in the model tank

Fig. 7 Sodium iodide solution

The grain size distribution for fused silica refers to sand gradation in the Yufuhe River of Jinan (Rong 2017). The particle distribution curve is shown in Fig. 8. To reduce the grain size effect, $D/d_{50} > 50$ (D is the tunnel diameter; d_{50} is the mean gravel size of sand) should be greater than 175 (Kirsch 2010) and $D/d_{50} = 187.5 > 175$ for the transparent gravel soil used in this paper. The direct shearing test is conducted on the fused silica under this gradation, with Mohr's Circle for stress shown in Fig. 9.

3.4 Test procedures

1. Transparent clay and pore fluids were prepared.

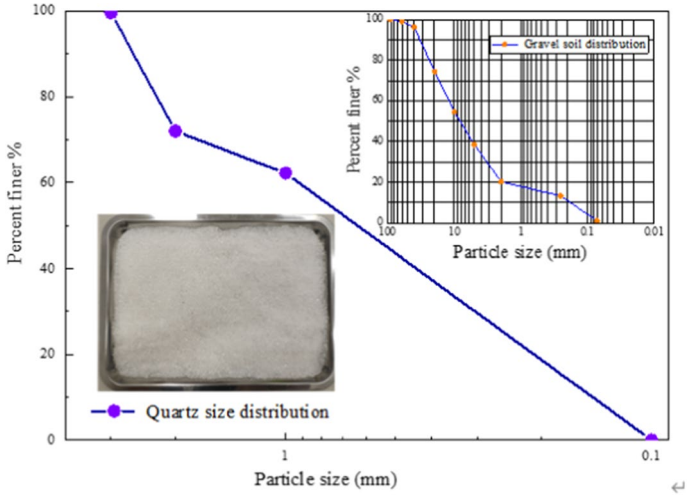

Fig. 8 Particle size distribution curve of fused quartz

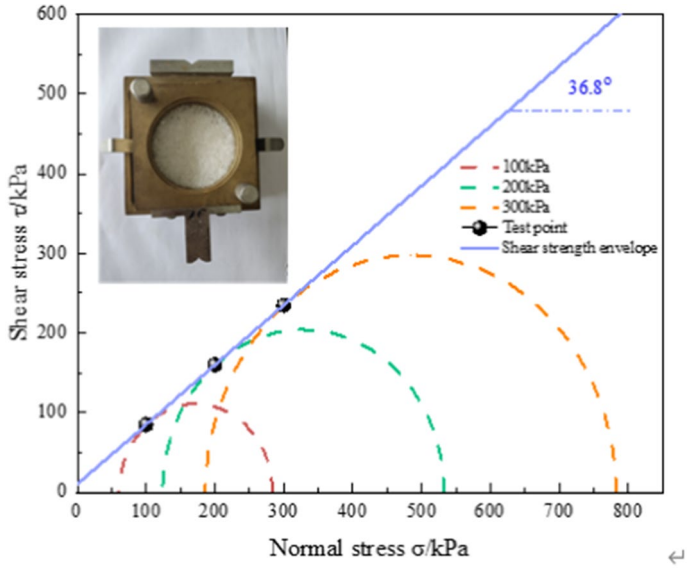

Fig. 9 Direct shearing test result of fused quartz

2. The fused quartz sand and pore fluids were filled into the model tank in layers and continuously stirred to remove air bubbles during the test.
3. The model tank, water tank, water pump, head control barrel and L-shaped water pipe with PUC pipe were connected. The water pump and valve were opened, and the valve sealing was checked. It was also confirmed whether the PUC pipe and equipment are in good condition.
4. The transparent clay was filled till the required height and allowed to rest for two days.

5. The CCD industrial camera and laser were fixed on a high-precision linear platform. Before the test, it was ensured that the section formed by the centerline of the light source was vertical. The tunnel symmetry plane was aligned. Also, the camera rubber ring and focal length were adjusted to obtain clear speckle images. To prevent light from causing errors in the test, carry out the test in a dark indoor environment.
6. The water pump was turned on and waited until the water level in the model tank and the liquid level in the head control barrel remained constant, showing that they achieved a stable seepage state.
7. The movement speed was set to 0.05 mm/min in the whole test (Liu et al. 2018), while the total horizontal displacement of the rigid plate was set to 20 mm, and the displacement increment was set to 0.25 mm until the total displacement reached 6.00 mm. For the remaining 14 mm of displacement, the incremental step was 0.50 mm (Kirsch 2010). For every 1 mm of retraction, rest for 20 min to bring it to a steady state. After the soil reached a stable state, the industrial camera and laser were controlled to move synchronously to capture images of different slice locations. The images of different slice locations were processed and analyzed through PIV technology to obtain the displacement fields of different slices.
8. The self-compiled 3D reconstruction program was used to reconstruct the displacement field and accurately obtain the stratum deformation in 3D space.

4 3D fluid–structure coupling model

To further study the instability and deformation, stress change of soil mass, and limit support pressure of tunnel face caused by the instability of tunnel face, based on the previous physical model test, the complete seepage stress module considering two-way fluid–structure interaction was used to simulate the water burst and seepage deformation of soil mass on the tunnel face. It was then analyzed and compared with the model test.

4.1 Establishment of finite element model

The dimensions of the overall finite element model were 0.85 m × 0.22 m × 0.51 m (length × width × height). The outer diameter of the tunnel was 0.12 m; the thickness of the tunnel sidewall was 0.006 m, and the distance between the tunnel face and the model boundary was 0.300 m. The dimensions were consistent with those of the model test area. The overall model is shown in Fig. 10.

Since the moving speed of the rigid plate in the model test is 0.05 mm/min, which is relatively slow, the instability of the tunnel face can be regarded as a quasi-static process (Liu et al. 2018). In this paper, the instability of the tunnel face is simulated by applying forced displacement to the excavation faceplate. Table 3 shows the detailed simulation scheme as follows:

4.2 Boundary conditions

(1) Boundary conditions for displacement

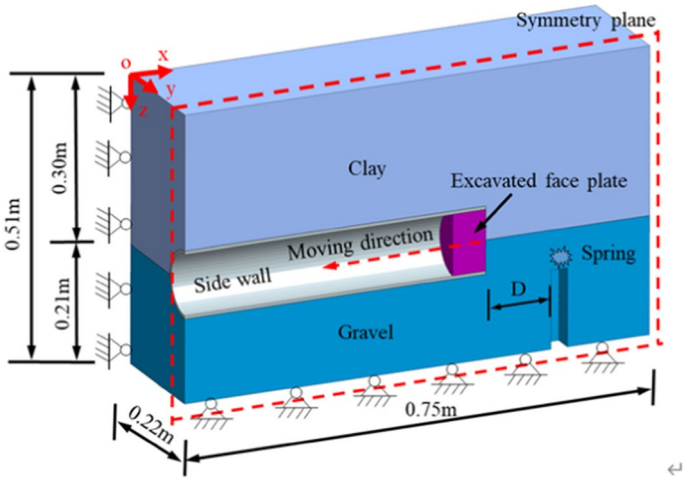

Fig. 10 Three-dimensional numerical model

Table 3 Simulation schemes

	Schemes	Stratum	Burial depth C/ tunnel diameter *D*	Spring head *H*/mm	Pipe diameter (mm)
Simulation schemes	1	Clay-Gravel	2.0	Not spring	–
	2	Clay-Gravel	2	5D	6.00
	3	Clay-Gravel	2.0	7D	6.00
	4	Clay-Gravel	2.0	9D	6.00
	5	Clay-Gravel	1.0	5D	6.00
	6	Clay-Gravel	0.5	5D	6.00

The boundary constraint conditions were the same as those during the test. The model's bottom boundary surface was a fixed boundary; the model's front and back boundary surfaces were subjected to displacement constraints in the *x*-direction; the model's left and right boundary surfaces were subjected to displacement constraints in the *y*-direction, and the upper surface was free boundary surface.

(B) Boundary conditions for seepage

The tunnel face was set as a seepage surface with zero pore water pressure. The other boundary surfaces were non-seepage surfaces. In the model, the groundwater level is located at the height of the soil interface.

(C) Boundary conditions for spring

The thickness of transparent clay layer is large, with low permeability, and the groundwater flow is concentrated in the transparent sand. In order to simulate the existence of spring in

the composite strata, the water head boundary of the corresponding working condition is set at the location of spring exposure. Set the seepage boundary condition with a head of 0 because the seepage occurs at the tunnel face. So, the ground water at the spring exposure will move toward the tunnel face under the condition of water head difference.

(D) Soil interface

During the test, in order to prevent the influence of pore fluid on the transparency of transparent sand, transparent clay and transparent sand are separated by a layer of film. In the process of numerical simulation, since the permeability coefficient of transparent clay is 1×10^{-7}, which is different from that of transparent sand by several levels, it is reasonable to set the interface between the two layers where seepage cannot occur.

4.3 Physical and mechanical parameters

In the simulation process for the instability of the tunnel face, the classical Mohr–Coulomb model was used as the soil model, and the soil mass, sidewall, and rigid excavation faceplate are all 3D solid elements. Table 4 shows the physical parameters of fused quartz and transparent clay (Guzman et al. 2014; Wallace and Rutherford 2015).

5 Analysis of test and simulation results

5.1 Support pressure ratio

The support pressures on tunnel face under the condition of spring with different confined water heads ($H/D=0$, 5, 7 D and 9) are obtained as shown in Fig. 11. The hollow points represent test results, while the solid lines represent numerical simulation results. In the picture, σ_0 is defined as total pressure of tunnel face at initial state, σ_S is defined as actual support pressure after tunnel face retreats. The rigid tunnel plate is connected with sensor. The combined axial force of the tension–compression sensor shaft is obtained through the tension–compression sensor. The tension–compression sensor is subjected to uniform pressure. The computer converts it into stress to obtain the support stress of the corresponding working condition.

Table 4 Material properties

	Unit weight (kN/m^3)	Cohesion (MPa)	Internal friction angle (°)	Elastic modulus (MPa)	Poisson ratio	Permeability Coefficient (m/s)
Clay	19.8	0.555	11	0.02	0.3	1×10^{-7}
Gravel	22	0	36.8	72,000	0.3	0.001
Excavated face plate	78.5	–	–	206,000	0.3	–
Side wall	78.5	–	–	206,000	0.3	–

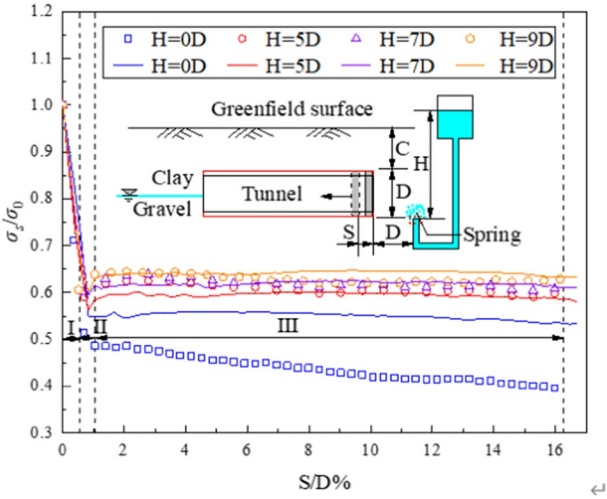

Fig. 11 Support pressure versus displacement of tunnel face (Different confined water head)

Under the condition of spring, the support pressure undergoes the following three stages: In the first stage, the tunnel face suddenly becomes unstable, and the support pressure decreases sharply from the static earth pressure at the initial time to the minimum value, decreasing by about 55–65%; In the second stage, the rebound stage, the support pressure rebounds about 3.3–3.6%. This is due to the large permeability of gravel and the gravel is relatively loose. Under the action of confined water, water flows to the tunnel face, and small gravel soil particles pour into the tunnel, causing an increase in support pressure (Kirsch 2010; Chen et al. 2013). In the third stage, with the further movement of the tunnel face, the equilibrium state of soil mass is broken, and the soil mass is subjected to plastic failure, forming an unstable area. The stress in soil mass in the unstable and deformed area does not change, and the support pressure on the tunnel face remains constant. In this case, the support pressure can be regarded as the limit support pressure, with the value increasing with the increase of confined water heads of the spring. According to the hydraulic calculation for long pipes, the flow velocity of spring water exhibits the following relationship with the confined water heads of spring, as shown in Eq. (1).

$$H = \lambda \frac{l}{d} \cdot \frac{v^2}{2g} \tag{1}$$

where λ—friction factor of head loss; l—pipe length (m); d—pipe diameter (m); v—flow velocity (m/s).

It can be obtained from the above formula that the increase of confined water head increases the velocity of spring water flowing to the tunnel face. Under the impact of spring, more small particles of gravel soil move toward the tunnel face, so the seepage force acting on the tunnel face increases. As a result, the support pressure on the tunnel face increases with the increasing spring's confined water head. However, the support pressure curve under the condition without spring is different from that obtained under the spring condition. It is mainly divided into a rapid decline stage and a slow decline stage, without a rebound stage.

Figure 12 shows the support pressure curves of the tunnel face under different burial depths ($C/D = 0.5$, 1.0, 2.0) when the shield excavation face is close to the spring. Tunnel

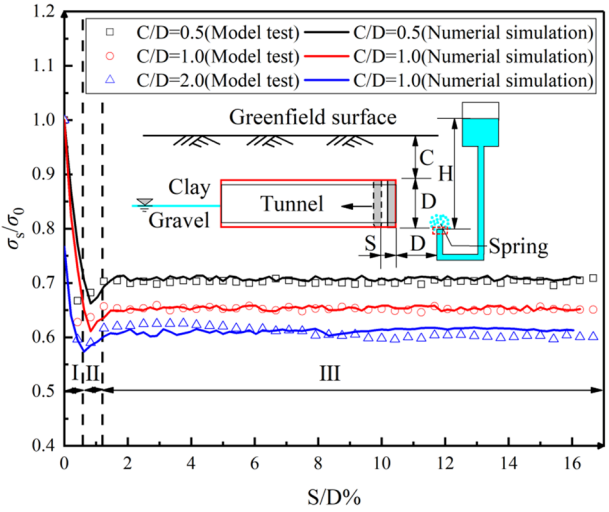

Fig. 12 Support pressure versus displacement of tunnel face (Different burial depth)

burial depth has no effect on the change law of the support pressure, but only affects the limit support pressure ratio. The change of the support pressure can still be divided into three stages: rapid decline, rebound stage, and stability. When the burial depth is relatively small, the effect of soil arch is weakened, the loose deformation of the surrounding strata increases, and the ultimate support pressure to stabilize the tunnel face becomes larger. When the burial depth is relatively large, the effect of soil arch is more significant, and the shear strength of the surrounding strata is fully exerted. The change of the support pressure ratio in the first stage is large, but the ultimate support pressure ratio gradually stabilizes as the instability deformation increases. The ultimate support pressure ratio of the tunnel face is 0.698, 0.650, and 0.603, respectively ($C/D = 0.5$, 1.0, 2.0).

5.2 Instability model of tunnel face

(a) Different pressure-bearing heads H

The high-definition images are processed by PIV technology to obtain soil displacement fields under the condition of spring with different confined water heads, as shown in Fig. 13. Initially, the area affected by the instability of the tunnel face is mainly concentrated in the clay, and the deformation of clay is more severe than that of gravel. As the rigid panels retreat, the instability zone gradually extends to the ground surface. When the rigid plate retreats by 1 mm, the equilibrium state of soil mass on the tunnel face is subjected to more disturbances under the condition of spring. In contrast, it is subjected to no disturbance under the condition without spring. When the rigid plate retreats by 3 mm, the failure zone of soil further expands. When it retreats by 6 mm, the failure zone of soil has extended to the ground surface under the condition with spring, but the surface displacement is close to 0 under the condition without spring. The failure zone of soil under the condition with spring is larger than that without spring.

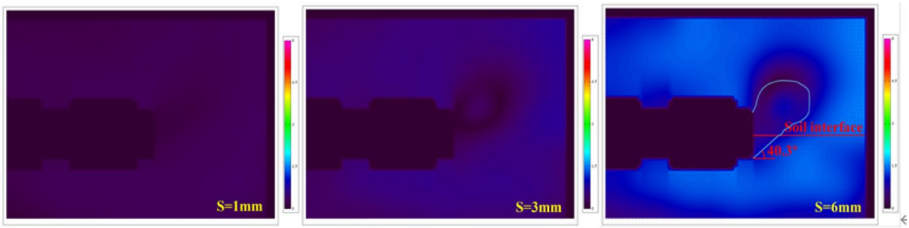

(a) No spring (C/D=2.0)

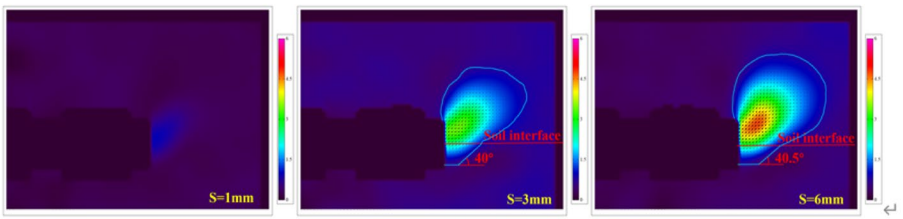

(b) H/D=5.0 (C/D=2.0)

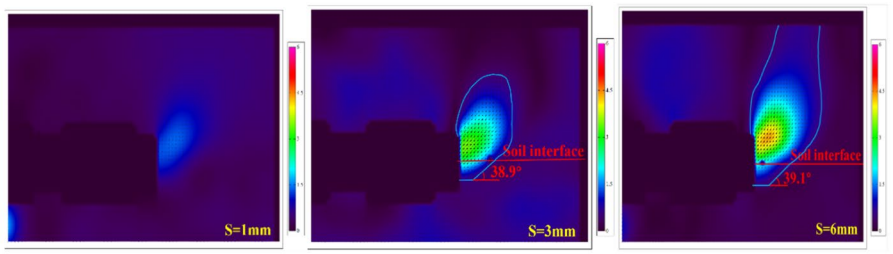

(c) H/D=7.0 (C/D=2.0)

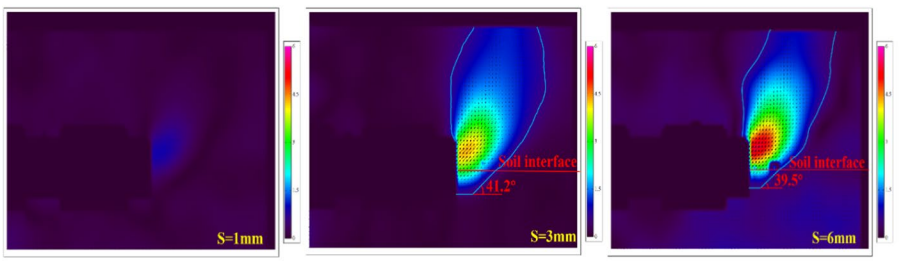

(d) H/D=9.0 (C/D=2.0)

Fig. 13 Evolution of the displacement fields (Different confined water head of spring)

It can be seen from Fig. 13 that the presence or absence of spring has a greater effect on the instability failure mode of the tunnel face. Under the condition without spring, the failure mode presents the combination of silo and wedge shapes. However, under the condition of spring, the failure mode of the gravel layer exhibits a "inverted prism" instead of a "wedge shape", and the lower boundary of the failure zone in the gravel layer is nearly a horizontal line segment. Meanwhile, the unstable area of the gravel layer forms an angle with the interface of the soil layer. The presence of spring has no significant effect on

the inclination angle. The inclination angle is approximately in the range of 39.0°–41.0°, which is smaller than the failure angle $\pi/4+\varphi/2$. (Liu et al. 2018).

(b) Different tunnel burial depth ratio C/D

Figure 14 shows the soil displacement field for the instability of the tunnel face at different buried depths under the condition of springs. When the horizontal displacement of the tunnel face is $S=1$ mm, the instability area is concentrated in clay. In the case of a large tunnel burial depth, due to the soil arch effect, the soil instability is mainly local deformation, and the surface is basically undisturbed. However, under the condition of $C/D=0.5$, there is an obvious instability area, and the ground deformation has developed from local instability to overall collapse. When $S=3$ mm, the plastic zone further develops to the surface. The smaller the C/D, the faster the instability zone develops, and the soil displacement becomes larger. Such as $C/D=0.5$, 1.0 conditions, the surface has appeared obvious displacement; When $S=6$ mm, under the shallow burial depth ($C/D=0.5$, 1.0), the instability deformation has developed into an overall collapse, and there is a large-scale instability collapse in front of the tunnel face. However, due to the effect of soil arching, $C/D=2.0$ working condition is still dominated by local instability.

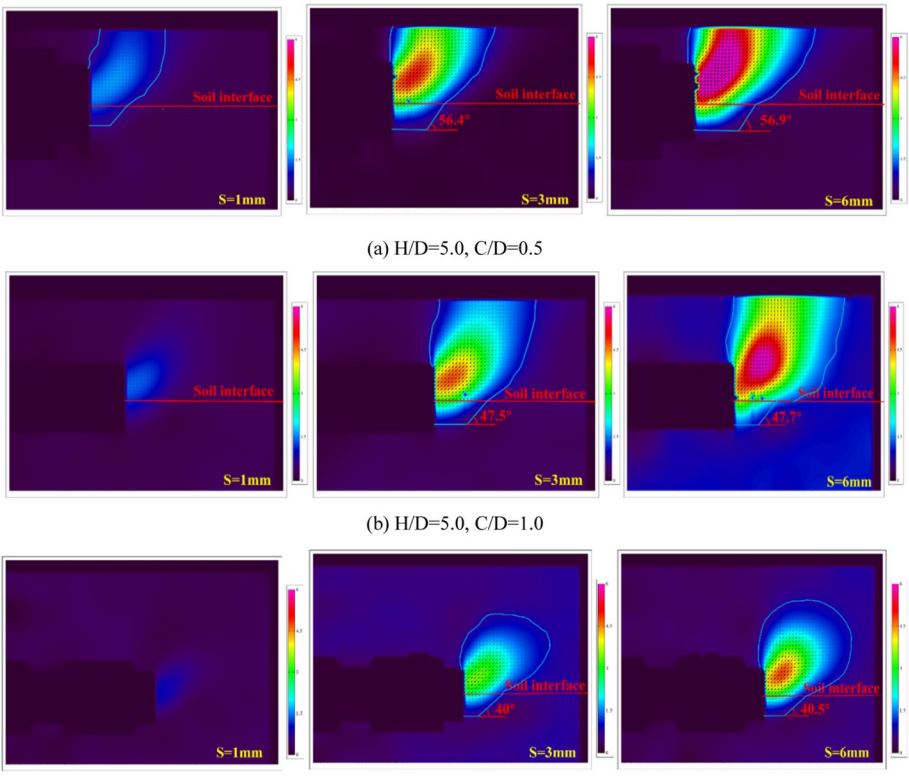

Fig. 14 Evolution of the displacement fields (Different tunnel depth)

The tunnel burial depth has no significant effect on the instability failure model, and its influence on the stratum is mainly reflected in the change of the instability zone and the instability displacement. Under the spring condition, the failure modes are "silo shape" and "inverted prism" combination. The angle between the instability zone of the gravel layer and the horizontal direction is also different. It increases nonlinearly with the decrease of the burial depth. The inclination angles are 56.9°, 47.7° and 40.5° under the conditions of $C/D = 0.5$, 1.0 and 2.0, respectively.

5.3 Contour map for soil displacement

Through the image processing software, the contour map of soil displacement (when the tunnel face retreats by 6 mm) is obtained under the spring conditions, as shown in Fig. 15. Since the disturbance degree of clay is larger than that of gravel, the instability areas are concentrated in the clay, and the maximum displacement occurs at D/4–D/2 away from the tunnel's central axis, indicating that the instability and deformation start from the center of the half-section on the tunnel face. Spring has a significant effect on the failure mode of soil. The unstable area of the clay layer extends to the surface in a "silo shape". The unstable area of the gravel layer develops to the interface of the soil layer in a "inverted prism". The lower boundary of the unstable area is a nearly horizontal straight line. With the increase of the confined water head, the loosening deformation continues to develop to the surface, the instability area is further expanded, and the surface impact range is also increasing. Under the condition of spring with the confined water head $H \geq 5$D, the increased confined water head causes the maximum displacement of the ground surface to increase from 0.58 to 1.40 mm.

Comparing Fig. 15b, e, f, it can be found that if there is a spring in front of the tunnel face, the smaller the thickness of the overlying soil layer on the tunnel, the more susceptible the surrounding strata is to the disturbance of the tunnel face instability, and the plastic area expands and the displacement increases. When the tunnel burial depth deeper, due to the effect of soil arch, the surrounding strata can fully exert its shear strength, thereby weakening the degree of disturbance of the surrounding strata by spring, and the instability displacement is relatively small. However, when the burial depth is shallow ($C/D = 0.5$, 1.0), large-scale collapse occurs in front of the tunnel face, and the soil in the area of about 0.293 D^2 and 0.037 D^2 had buckling displacement greater than 6.00 mm.

5.4 Soil displacement in front of tunnel face

To further explore the relationship between the soil displacement on the tunnel face and the confined water head of spring, the soil displacements at $L = 0$ D and 0.25 D in front of the tunnel face are also monitored, as shown in Fig. 16. Figure 16 shows the soil displacement of 0 D and 0.25 D in front of the tunnel surface obtained by numerical simulation. In the figure, L is defined as the horizontal distance between monitoring line and tunnel surface. Under the condition with spring, the clay displacement on the tunnel face is significantly larger. The increase in the confined water head greatly increases the seepage force on the tunnel face, which further aggravates the instability and deformation of the clay and gravel layers on the tunnel face. In terms of the soil on the tunnel face, the maximum displacement appears at different locations, and the maximum displacement appears at the interface of the soil layer under the condition without spring. However, under the condition with spring, the maximum displacement position of the tunnel face moves toward the top of the

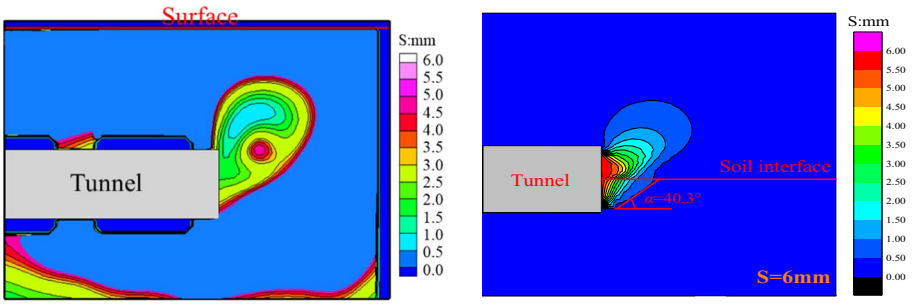

(a) Not Spring, C/D=2

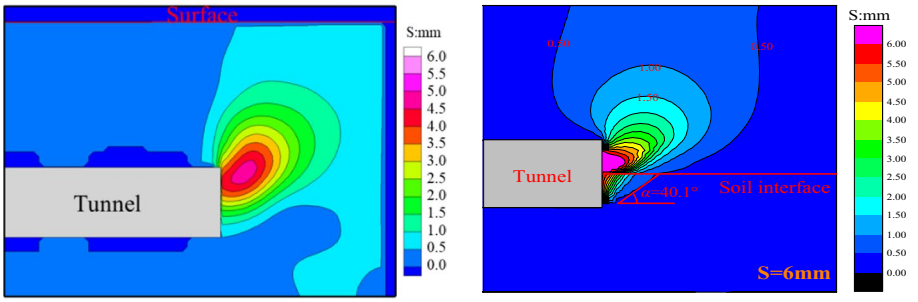

(b) H/D=5.0, C/D=2.0

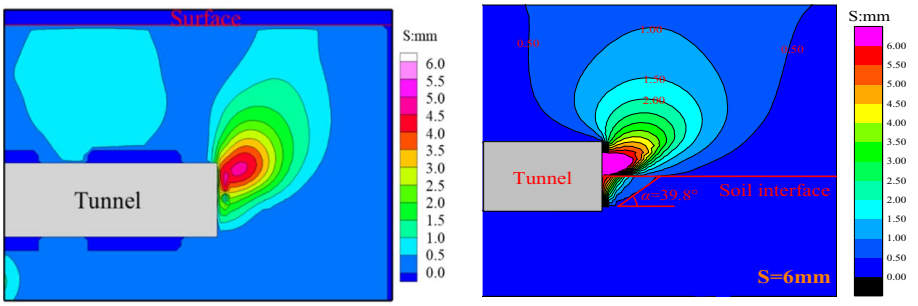

(c) H/D=7.0, C/D=2.0

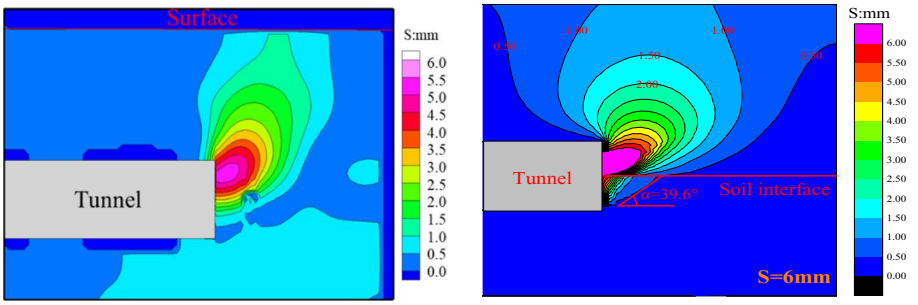

(d) H/D=9.0, C/D=2.0

Fig. 15 Deformation contour map (The left and right figures show the model test results and numerical simulation results, $S = 6$ mm)

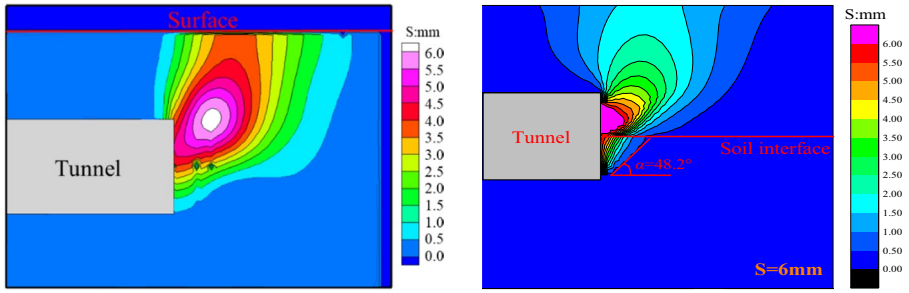

(e) H/D=5.0, C/D=1.0

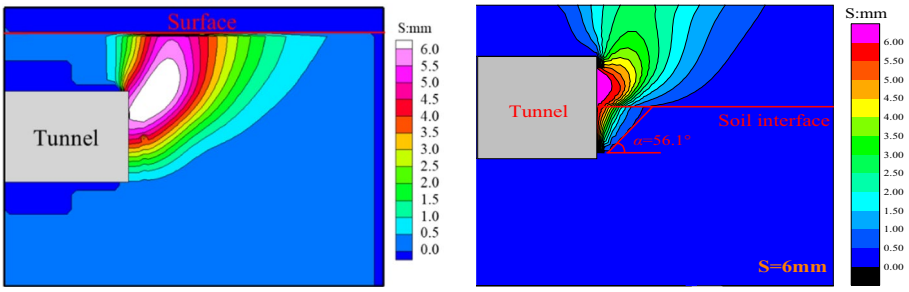

(f) H/D=5.0, C/D=0.5

Fig. 15 (continued)

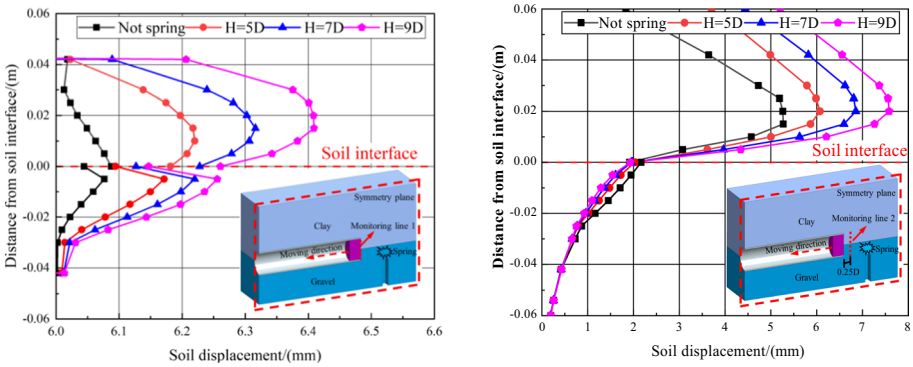

(a) L=0 (b) L=0.25D

Fig. 16 Curve of soil displacement (Simulation results, Different confined water head of spring, S = 6 mm)

tunnel. The maximum displacement occurs at 0.17 D above the tunnel axis under the condition of H/D = 9.0. Due to the severe deformation of clay on the tunnel face, the overlying earth pressure on the gravel layer increases, so the gravel becomes more compact. Meanwhile, the deformation of clay on the tunnel face exerts reaction force toward the tunnel's outward direction on the lower gravel layer. Therefore, with the increase of the confined water head H of spring, the deformation of the gravel layer at 0.25 D in front of the tunnel face exhibits a declining trend.

Figure 17 shows the displacement curves of the soil in front of the tunnel face under different burial depth ratios. Figure 17 shows the soil displacement of 0 D and 0.25 D in front of the tunnel surface obtained by numerical simulation. In the figure, L is defined as the horizontal distance between monitoring line and tunnel surface. It can be seen that the variation law of soil displacement of the tunnel face at different positions with the buried depth of the tunnel is different. At 0.125 D above the central axis, the buried depth ratio changes, the soil displacement basically does not change. Below this position, due to the influence of the overburden pressure, with the increase of the burial depth ratio, the soil in this area is more prone to loosening and deformation to the excavation surface of the tunnel. Above the turning point, when the burial depth is relatively large, the soil arching effect is more significant, and the upward development of the plastic zone slows down. In the case of $C/D = 0.5$, the clay displacement at $L = 0.25$D in front of the tunnel face is smaller than that in the case of $C/D = 1.0$ and 2.0, but the instability displacement of the gravel layer below is not much different.

5.5 3D space stratum deformation

In the model test, Gaussian filtering is adopted. The value of each pixel in the window is weighted and averaged by its own and other neighboring pixel values (Lin and Luo 2006). First, linear interpolation is performed on adjacent images to make the reconstructed contour smoother. After linear interpolation, in order to make the reconstruction model more accurate, the cubic B-spline interpolation method is used to re-process the image (Lee et al. 1997). Finally, based on the ray casting algorithm, the adaptive modeling method is used to simulate more detailed areas (areas with more complex model boundaries).

Through a self-compiled 3D reconstruction program, the displacement fields at different slices are reconstructed to obtain a 3D soil instability failure model, as shown in Fig. 18. Compared with the cloud map presenting 2D deformation, the soil failure mode can be observed more intuitively from 3D space. When there is a spring in front of the tunnel face, the soil's unstable area develops to the ground surface, and the disturbance to soil is more significant, with the deformation of clay being the largest. Under the working condition without spring, the influence area in the lower gravel layer is much smaller than that under the condition with spring. The instability of the tunnel face does not cause

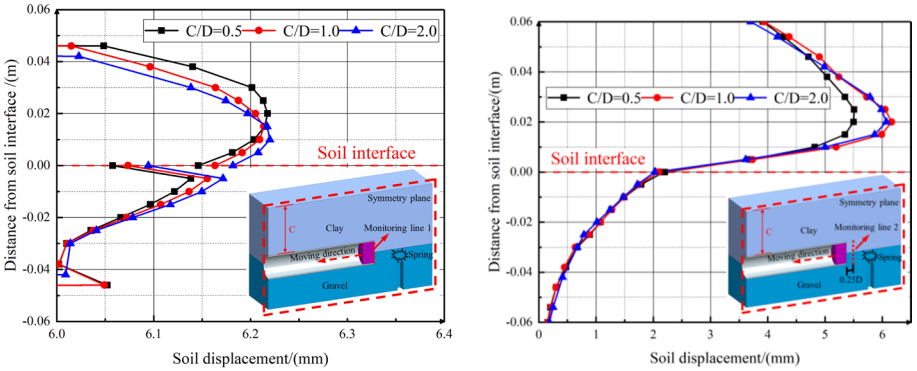

Fig. 17 Curve of soil displacement (simulation results, different tunnel depths, $S = 6$ mm)

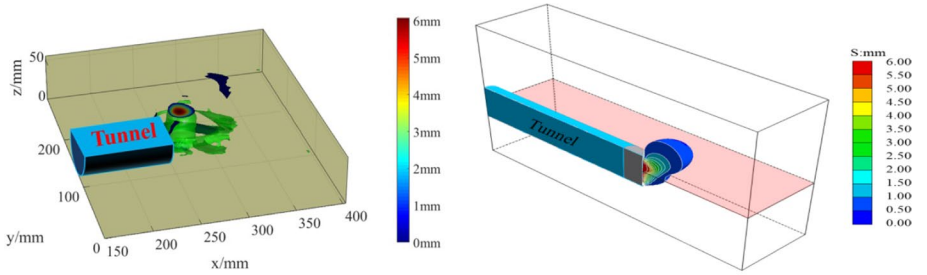

(a) Not Spring, C/D=2.0

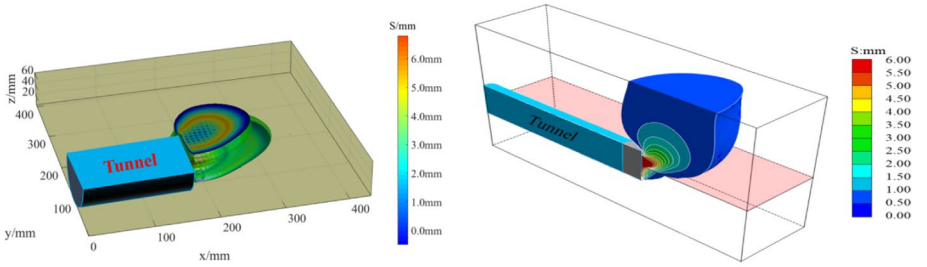

(b) H/D=5.0, C/D=2.0

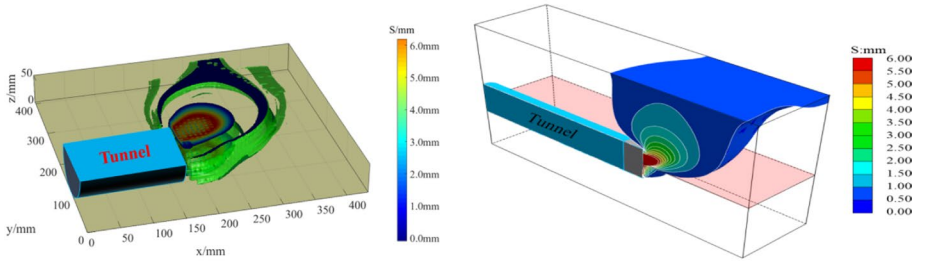

(c) H/D=7.0, C/D=2.0

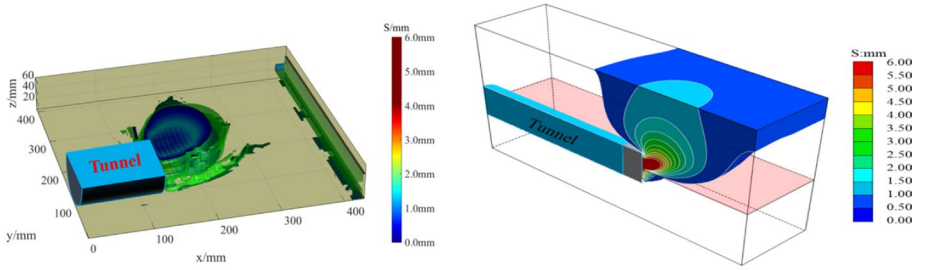

(d) H/D=9.0, C/D=2.0

Fig. 18 The three-dimensional reconstruction view on the failure zone (The left and right figures show the model test results and numerical simulation results, $S = 6$ mm)

significant disturbance to the ground surface. From the reconstruction images, it is clear that there are differences in the shape of the damaged body model for soil mass on the tunnel face under the conditions with spring and without spring. Under the condition without spring, due to the clay's soil arching effect, the failure area does not develop to the ground

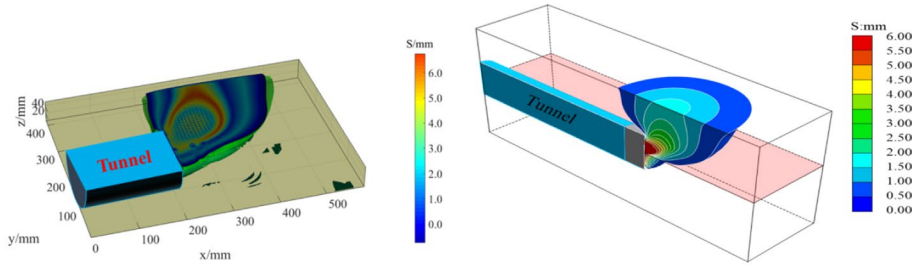

(e) H/D=5.0, C/D=1.0

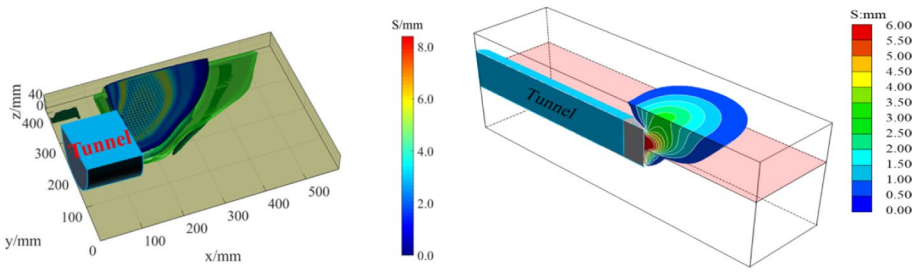

(f) H/D=5.0, C/D=0.5

Fig. 18 (continued)

surface. The instability failure model is composed of a funnel and wedge. When there is a spring in front of the tunnel face, the instability failure model develops to a funnel shape and inverted prism, and the failure zone develops to the ground surface. With the increase of the spring's confined water head, the failure area gradually expands. Comparing the 2D displacement field image obtained by the traditional image measurement technology with the 3D-reconstructed image, it can be found that the instability of the tunnel face under the condition with spring is a 3D issue.

Comparing with Fig. 18b, e, f, it can be seen that if there is a spring in front of the shield, the tunnel burial depth has no significant effect on the 3D failure model shape of the surrounding strata. The effect of the change in burial depth ratio on the surrounding strata is mainly reflected in the destabilization displacement and the failure zone. When the burial depth is small, the instability of the tunnel face causes huge disturbance to the surrounding strata, and the loose deformation of the soil will increase. However, the greater the burial depth, the more significant the soil arch phenomenon resulting in relatively small instability deformation.

5.6 Analysis of the soil stress in front of tunnel face

The instability of the tunnel face breaks the original equilibrium state, and the stress on soil mass has been redistributed. The relationship between the vertical stress σ_{zz} of soil and the retreat displacement S of the tunnel face under different working conditions is shown in Fig. 19. It can be seen that under the condition of no spring, the deformation of the stratum is dominated by loose deformation. The vertical stress in the clay has been decreasing at a steady rate as the horizontal displacement of the tunnel face increases. When the shield excavation surface is close to the spring, the vertical stress σ_{zz} in clay of the tunnel face

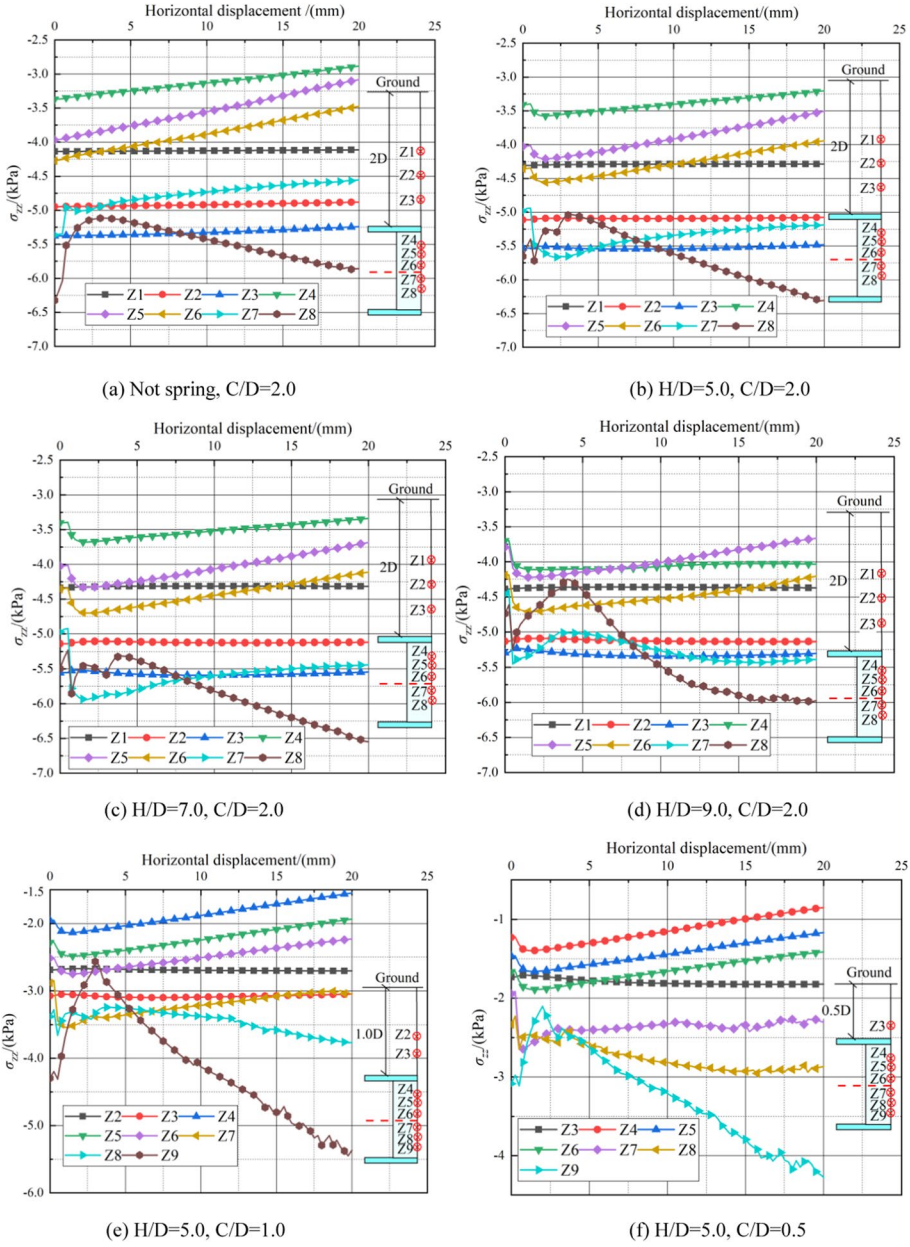

Fig. 19 Soil vertical stress versus horizontal displacement of tunnel face

has experienced two changing stages: (1) At the initial moment, the loose deformation is small due to the effect of soil arch, and the vertical stress σ_{zz} of the excavation surface clay increases slightly. (2) As the rigid panel continues to retreat, it makes the plastic zone of the soil expands, and the vertical stress σ_{zz} of the soil keeps decreasing. This may be due to the instability deformation and plastic failure zone when the retraction displacement is

large. The larger the spring confining head H, the faster the buckling deformation and the development rate of the buckling zone, the weaker the soil arching effect, and the smaller the reduction of the soil vertical stress. With the increase of the confining head H, the instability deformation and the development rate of the failure zone are accelerated. Ultimately, the weakening of the soil arch effect is manifested in the reduction of the vertical stress of the soil becomes smaller.

For the gravel layer, the stress change at the interface of the soil layer is similar to the clay. However, the closer to the bottom, the vertical stress first decreases and then increases as the horizontal displacement of the tunnel face increases. At the beginning of the tunnel face instability, the vertical stress of soil decreases. In the later stage of excavation surface instability ($S \geq 5$ mm), the deformation of the gravel layer reaches stability, and the vertical earth pressure of the bottom gravel layer is greater than the initial value.

Comparing Fig. 19b, e, f, it can be seen that there is no significant difference in the vertical stress of the soil under different burial depths. When the tunnel burial depth is smaller, the increment of vertical stress in the clay soil at the excavation surface becomes larger in the early stage and decreases in the later stage. Near the interface of the soil layer, the vertical stress variation law of gravel is similar to that of clay. However, the closer to the tunnel sidewall, the greater the burial depth ratio, the larger the vertical stress increment becomes. This is because the thickness of the overlying soil layer is larger and the pressure on the gravel increases, which intensifies the loose deformation of the gravel. When $C/D \geq 1.0$, the vertical stress of the overlying clay basically does not change as the horizontal displacement of the tunnel face increases, but it has a slight decreasing trend under the condition of $C/D = 0.5$.

Figures 20 and 21 are the vertical stress σ_{zz} and horizontal stress $(\sigma_{xx} + \sigma_{yy})/2$ curves of the clay under different working conditions. In the picture, σ_{xx} is defined as horizontal stress of soil mass in the x-direction, σ_{yy} is defined as horizontal stress of soil mass in the y-direction. The pore water pressure at the tunnel face of the tunnel is zero, and the soil undergoes large seepage deformation. Therefore, the soil stress at the tunnel face is smaller than that in other locations. Loose deformation occurs in the clay area close to the excavation surface, and the vertical stress of the soil gradually decreases with the increase of the instability degree of the tunnel face. The higher the pressure head is, the smaller the stress increment becomes. The vertical stress of the clay increases with the distance from the tunnel face, which may be due to the influence of the continuous transmission of the soil arching pressure. If there is no influence of spring, the turning point of stress change is 0.09 m away from the tunnel face, and if there is a spring, it is 0.05–0.06 m. When there is a spring or not and the water head of the spring changes, the soil arch effect appears at 0.83 D above the tunnel vault, and there is no obvious extension. Regardless of the existence of springs and the change of the confined water, the soil arch effect appears at 0.83 D above the tunnel vault. The change of the horizontal stress of the clay in front of the tunnel face ($Z = -0.285$) is similar to the vertical stress. The soil pressure in the horizontal direction of the overlying clay is significantly affected by the instability of the tunnel face, and it gradually increases with the increase of the stratum loss. The higher the spring confined water head, the larger the horizontal stress increment.

When the tunnel buried depth is small, the surrounding strata are more prone to loosening and deformation, the plastic zone develops to the surface and continues to expand. The vertical stress reduction of the soil in the loosened area becomes smaller, and the vertical stress increment in the distance becomes larger. The height of the loosening area is different under different buried deep spring conditions. When the tunnel burial depth is $C/D = 0.5$, 1.0 and 2.0, the soil arch effect occurs at the top of the tunnel 0.17 D, 0.50 D,

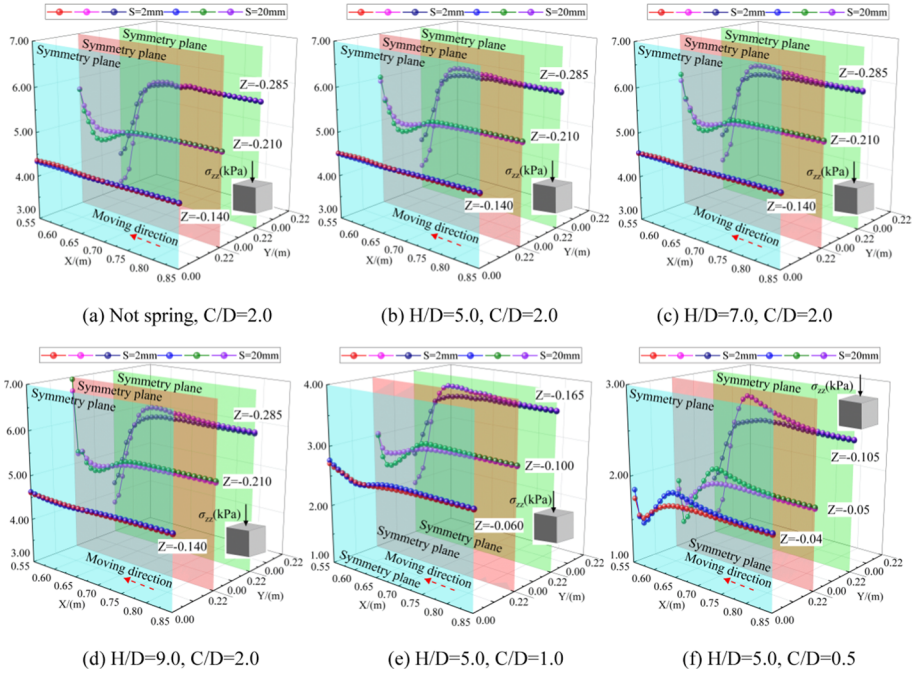

(a) Not spring, C/D=2.0 (b) H/D=5.0, C/D=2.0 (c) H/D=7.0, C/D=2.0

(d) H/D=9.0, C/D=2.0 (e) H/D=5.0, C/D=1.0 (f) H/D=5.0, C/D=0.5

Fig. 20 Variation of soil vertical stress

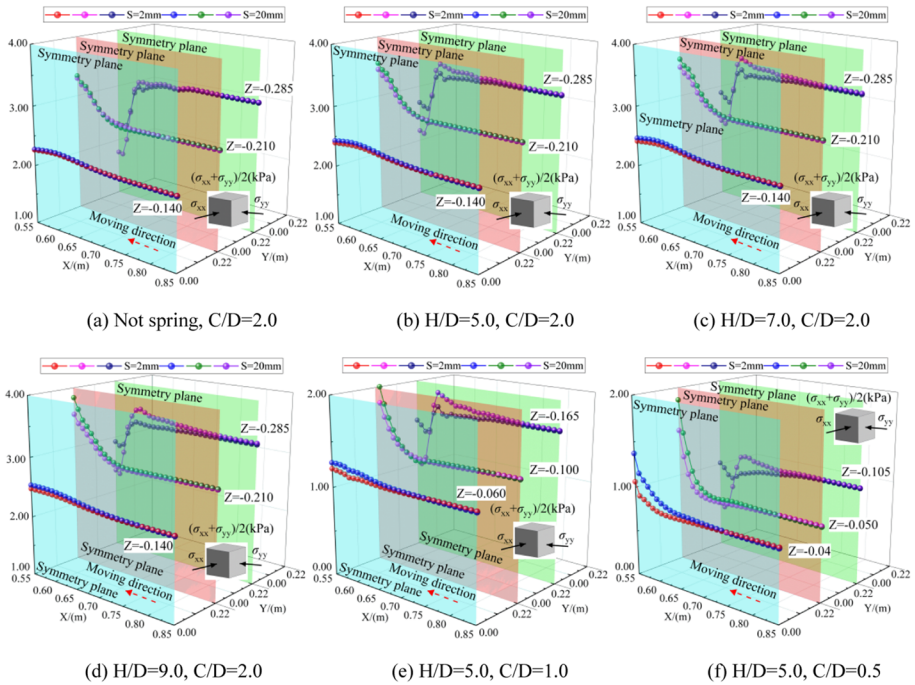

(a) Not spring, C/D=2.0 (b) H/D=5.0, C/D=2.0 (c) H/D=7.0, C/D=2.0

(d) H/D=9.0, C/D=2.0 (e) H/D=5.0, C/D=1.0 (f) H/D=5.0, C/D=0.5

Fig. 21 Variation of soil horizontal stress

0.83 D, respectively. When the tunnel is buried deeper, the dominant soil arch expands outward continuously, and the ultimate support pressure required for the occurrence of overall instability is reduced. The deeper the tunnel is buried, the more significant the soil arching effect is, and the horizontal stress increment of the overlying clay becomes smaller. The specific realization is that after the instability of the tunnel face reaches stability, the damage will not develop further.

6 Conclusions

In this paper, we study the existence of spring along the tunnel on the failure mode of instability and the impact of the ultimate support pressure. Through the tunnel face stability model device, six groups of tunnel face progressive instability model tests under the condition of springs were carried out. Combined with CT scanning, image measurement and 3D reconstruction technology, 2D and 3D failure models under different conditions were obtained, and the influence of spring confined water head and tunnel buried depth was discussed. Finally, six sets of 3D finite element analysis of the same working conditions were carried out.

The following conclusions are drawn from this study.

(1) Initially, support pressure is rapidly declines from the static earth pressure to the minimum value. With the retreat of the rigid panel, the support pressure will rebound and rise steadily under the spring condition, while it will remain stable without spring. The ultimate support pressure ratio increases with the increase of the spring confining head. When the shield working face is close to the spring, the deeper the tunnel is buried, the more significant the soil arch effect will reduce the support pressure.

(2) In the area with spring, the spring located in the tunnel interval significantly affects the instability and failure mode of soil mass. Under the condition without spring, the failure mode is the combination of "silo shape" and "wedge shape", without extending to the ground surface; In contrast, under the working condition with spring, the failure mode is composed of "silo shape" and "inverted prism", and obvious soil displacement has occurred on the ground surface. With the increase of the confined water head, more fine-grained gravel soil pours onto the tunnel face, so the soil deformation on the tunnel face increases, resulting in further expansion of the unstable and deformed area. When the burial depth of the tunnel is changed, the failure mode under the influence of the spring is still "silo shape and inverted prism". At large burial depths, the plastic zone develops slowly.

(3) Under different working conditions, the maximum displacement of the tunnel face soil appears in different positions. In the absence of springs, it appears at the soil layer interface. If there is a spring, the maximum displacement will move to the top of the tunnel with the increase of the pressure head of the spring. The soil displacement of the tunnel face at 0.125 D above the central axis remains basically unchanged as the tunnel burial depth changes. Above it, the soil displacement decreases with the increase of the burial depth due to the soil arching effect. Below it, the soil displacement increases with the buried depth of the tunnel due to the overlying soil pressure.

(4) The vertical stress of soil at different positions varies with the instability of the tunnel face. The vertical stress of the clay at the tunnel face increases first and then decreases, while the vertical stress of the gravel decreases first and then increases. In the loose

area, the vertical soil pressure decreases gradually with the increase of the instability degree at the tunnel face. Outside the loosening zone, it increases instead. With the presence or absence of springs and the change of spring water head, the soil arch effect appears at about 0.83 D above the tunnel vault. The deeper the tunnel is buried, the more significant the soil arching effect is, and the farther the soil arch effect occurs from the top of the tunnel.

Funding The authors would like to acknowledge the financial supports from National Natural Science Foundation of China (Nos. 52268062, 52278337 and 51968005) and Guangxi natural science foundation (No. 2022GXNSFBA035580) and the Guangxi Key Project of Nature Science Foundation (No. 2020GXNSFDA238024) and the Guangxi Natural Science Foundation (2019GXNSFBA185038) and the Key Research and Development Program of Guangxi (GUIKE AB22080061) and the Guangxi transportation industry key science and technology projects (GXJT-2020-02-08).

Declarations

Conflict of interest The authors declare that they have no known competing financial interests or personal relationships that could have appeared to influence the work reported.

References

Carvalho T, Suescun-Florez E, Omidvar M, Iskander M (2015) A nonviscous water-based pore fluid for modeling with transparent soils. Geotech Test J 38(5):805–811. https://doi.org/10.1520/GTJ20140278

Chen R, Li J, Kong L, Tang L (2013) Experimental study on face instability of shield tunnel in sand. Tunn Undergr Space Technol 33:12–21. https://doi.org/10.1016/j.tust.2012.08.001

Chen R, Yin X, Tang L, Chen Y (2018) Centrifuge model tests on face failure of earth pressure balance shield induced by steady state seepage in saturated sandy silt ground. Tunn Undergr Space Technol 81:315–325. https://doi.org/10.1016/j.tust.2018.06.031

Chen X, Zhang S, Zhou X, Xia P (2022) Parameter analysis of excavation face stability of shield tunnel under high water pressure seepage. Phys Chem Earth 128:103218. https://doi.org/10.1016/j.pce.2022.103218

Chini C, Wallace J, Rutherford C, Peschel J (2015) Shearing failure visualization via particle tracking in soft clay using a transparent soil. Geotech Test J 38(5):708–724. https://doi.org/10.1520/GTJ20140210

Dai C, Wang Q, Jiang K, Zheng T (2021) Ultimate Support Force of excavation face in curved shield tunnels in composite strata. Teh Vjesn Tech Gaz 28(3):708–717. https://doi.org/10.17559/TV-20180720050519

Ding X, Li K, Xie Y, Liu S (2022) Face stability analysis of large shield-driven tunnel in rock–soil interface composite formations. Undergr Space 7(6):1021–1035. https://doi.org/10.1016/j.undsp.2022.01.007

Guzman I, Iskander M, Suescun-Florez E, Omidvar M (2014) A transparent aqueous-saturated sand surrogate for use in physical modeling. Acta Geotech 9(2):187–206. https://doi.org/10.1007/s11440-013-0247-2

Iskander S, Sadek S, Liu J (2002) Optical measurement of deformation using transparent silica gel to model sand. Int J Phys Model Geotech 2(4):13–26. https://doi.org/10.1680/ijpmg.2002.4.13

Kirsch A (2010) Experimental investigation of the face stability of shallow tunnels in sand. Acta Geotech 5(1):43–62. https://doi.org/10.1007/s11440-010-0110-7

Lee S, Wolberg G, Shin S (1997) Scattered data interpolation with multilevel B-splines. IEEE Trans Vis Comput Gr 3(3):228–244. https://doi.org/10.1109/2945.620490

Li L, Tu W, Shi S, Chen J, Zhang Y (2016) Mechanism of water inrush in tunnel construction in Karst area. Geomat Nat Haz Risk 7:35–46. https://doi.org/10.1080/19475705.2016.1181342

Lin G, Luo L (2006) Accelerated Monte Carlo dose distribution simulation based on three-dimensional Gaussian filter denoising. Chin J Radiol Med Prot 26(4):389–390

Liu J, Iskander M (2010) Modeling capacity of transparent soil. Can Geotech 47(4):451–460. https://doi.org/10.1139/T09-116

Liu W, Zhao Y, Shi P, Li J, Gan P (2018) Face stability analysis of shield-driven tunnels shallowly buried in dry sand using 1-g large-scale model tests. Acta Geotech 13(3):693–705. https://doi.org/10.1007/s11440-017-0607-4

Liu C, Tang X, Wei H, Wang P, Zhan H (2020) Model tests of jacked-pile penetration into sand using transparent soil and incremental particle image velocimetry. KSCE J Civ Eng 24(4):1128–1145. https://doi.org/10.1007/s12205-020-1643-4

Lu X, Zhou Y, Huang M, Zeng S (2018) Experimental study of the face stability of shield tunnel in sands under seepage condition. Tunn Undergr Space Technol 74:195–205. https://doi.org/10.1016/j.tust.2018.01.015
Luo L, Wen H, Zheng R, Liu R, Li Y, Luo X, You Y (2019) Subaerial sulfate mineral formation related to acid aerosol at Zhenzhu Spring, Tengchong, China. Mineral Mag 83:381–392. https://doi.org/10.1180/mgm.2018.164
Ma S, Duan Z, Huang Z, Liu Y, Shao Y (2021) Study on the stability of shield tunnel face in clay and clay-gravel stratum through large-scale physical model tests with transparent soil. Tunn Undergr Space Technol 119:104199. https://doi.org/10.1016/j.tust.2021.104199
Ma S, Wei R, Shao Y, Huang Z, Duan Z (2021b) 3D visual model tests on stability of tunnel excavation surface based on transparent soil. Chin J Geotech Eng 43(10):1798–1806
Rong Q (2017) Study on the aquifer clogging along with the groundwater recharge by the yellow river water in the strong leakage area of the Yufu River. University of Jinan
Sui H, Ma C, Dai C, Yang T (2021) Study on stability of shield tunnel excavation face in soil–rock composite stratum. Math Probl Eng. https://doi.org/10.1155/2021/5579103
Sun S, Li L, Wang J, Shi S, Song S, Fang Z, Ba X, Jin H (2018) Karst development mechanism and characteristics based on comprehensive exploration along Jinan Metro, China. Sustainability 10:3383. https://doi.org/10.3390/su10103383
Tian Y (2018) Experimental observation and theoretical analysis on the Bubbles' shape within transparent soft soil. Zhejiang University
Wallace J, Rutherford C (2015) Geotechnical properties of LAPONITE RD. Geotech Test J 38(5):574–587. https://doi.org/10.1520/GTJ20140211
Wang G, Lyu H, Shen J, Lu L, Li G, Arulrajah A (2017a) Evaluation of environmental risk due to metro system construction in Jinan, China. Int J Environ Res Public Health 14(10):1114. https://doi.org/10.3390/ijerph14101114
Wang T, Zhan S, Chen C, Su W (2017b) Characterizing fractures to mitigate inrush of water into a shaft using hydrogeological approaches. Tunn Undergr Space Technol 61:205–220. https://doi.org/10.1016/j.tust.2016.10.011
Wang Y, Jing H, Yu L, Su H, Luo N (2017c) Set pair analysis for risk assessment of water inrush in karst tunnels. Bull Eng Geol Environ 76(3):1199–1207. https://doi.org/10.1016/j.tust.2021.103988
Wang G, Wu Y, Lu L, Li G, Shen J (2019) Investigation of the geological and hydrogeological environment with relation to metro system construction in Jinan. Bull Eng Geol Environ 78:1005–1024. https://doi.org/10.1007/s10064-017-1140-2
Yin X, Chen R, Meng F (2021) Influence of seepage and tunnel face opening on face support pressure of EPB shield. Comput Geotech 135(135):104198. https://doi.org/10.1016/j.compgeo.2021.104198
Zhang P, Pan Y, Yu Z, Guan X, Wang G, An J, Lei H (2020a) Ground subsidence characteristics caused by construction of shallow-buried tunnel in a sandy soil composite formation. Arab J Geosci. https://doi.org/10.1007/s12517-020-05880-z
Zhang Y, Hu M, Ye T, Chen Y, Zhou Y (2020b) An Experimental study on the rheological properties of laponite RD as a transparent soil. Geotech Test J 43(3):607–621. https://doi.org/10.1520/GTJ20180348
Zhao H, Ge L, Luna R (2010) Low viscosity pore fluid to manufacture transparent soil. Geotech Test J 33(6):463–468. https://doi.org/10.1520/GTJ102607

Authors and Affiliations

Shaokun Ma[1] · Hongye Wei[1] · Zhibo Duan[1,2] · Ying Liu[1] · Zhen Huang[1] · Benfu He[1] · Zhang Zhou[1]

✉ Zhibo Duan
duanzhibo_1993@163.com

Shaokun Ma
mashaokun@gxu.edu.cn

Hongye Wei
1175995423@qq.com

Ying Liu
lyily1112@126.com

Zhen Huang
hzcslg@163.com

Benfu He
1273200278@qq.com

Zhang Zhou
735435967@qq.com

[1] College of Civil Engineering and Architecture, GuangXi University, Nanning 530004, China

[2] Department of Civil Engineering, Tsinghua University, Beijing 100084, China